ELSEVIER

International Journal of Mass Spectrometry 208 (2001) 169–191

International Journal of Mass Spectrometry

Characterization of the ion-sampling pinhole interface for an ion mobility spectrometer/mass spectrometer system

Glenn E. Spangler*

Technispan LLC, 1133C Greenwood Road, Pikesville, MD 21208, USA

Received 12 October 2000; accepted 26 March 2001

Abstract

The pinhole interface to an ion mobility spectrometer/mass spectrometer (IMS/MS) is characterized by studying the water and nitrogen solvated ions $M^{\pm}(H_2O)_n(N_2 \text{ or } Ar)_m$ ($M^{\pm} = H_3O^+$, NH_4^+, O_2^-, O_4^-, or CO_4^-) produced in the IMS using purified air and argon carrier gases. The interface was found to distort the cluster distributions caused by shifting equilibria during gas expansion, followed by freezing of the equilibria. The nitrogen and argon adducts are not formed in the IMS, but are formed downstream from the Mach disc located within the vacuum system of the mass spectrometer. (Int J Mass Spectrom 208 (2001) 169–191) © 2001 Elsevier Science B.V.

Keywords: Ion-sampling; Ion mobility spectrometry

1. Introduction

Ambient pressure ion mobility spectrometry (IMS) has been applied to analyze volatile and semivolatile compounds in both the laboratory and the field [1–7]. In particular, it has been used to detect illicit drugs, explosives, and chemical warfare agents. For most of these applications, the ions formed in the IMS have been characterized using mass spectrometry (IMS/MS) [8–18]. Unfortunately, the ability of the mass spectrometer to identify ions has been questioned. The concern is that the ions are solvated and that the distribution of the solvated ions changes as the stagnant drift gas expands into the vacuum system of the mass spectrometer.

The ability of ions to attract and attach neutral molecules (i.e., condensation) is a subject with a long history. Wilson [19] was the first to demonstrate that ions can enhance nucleation phenomena. More recently, Searcy and Fenn [20] demonstrated that ion nucleation is involved in the formation of the hydrated hydronium, $H_3O^+(H_2O)_n$, ions. Because hydrated hydronium ions also make a major contribution to the reactant ions of ion mobility spectrometry [21], nucleation phenomena are expected to contribute to IMS/MS spectra that are recorded after a free jet expansion.

Searcy and Fenn [20] explain that a free jet expansion can be viewed as a fast flow reactor. This being the case, any ions entrained in the expanding buffer gas can change composition. Zook and Grimsrud observed that the degree of nucleation is dependent on the composition of the buffer gas [22]. When the buffer gas is helium or hydrogen heated to 125–250°C, the sampling errors are reduced so that

*E-mail: GSPAN@aol.com

1387-3806/01/$20.00 © 2001 Elsevier Science B.V. All rights reserved
PII S1387-3806(01)00433-X

relative ion intensities are essentially identical to those theoretically anticipated in the stagnant gas.

When Lee et al. [23] studied the IMS/MS spectra for protonated water clusters $H^+(H_2O)_n$ in helium ($n = 1, \ldots, 5$), they found that the relative ion intensities could be predicted using ab initio calculations combined with appropriate thermodynamic and statistical–mechanical procedures. Because their success was probably related to the lower water concentrations used in their experiments (1–91 ppm), they also tried to fit Zook and Grimsrud's [22] (water concentrations on the order of 6052–24,605 ppm) data with their ab initio approach. The agreement was quite good except for a slight discrepancy for the 24,605 ppm (18.7 Torr) data collected at 428 K. While the cause for the slight discrepancy was unknown, the computed results displayed the same general trends as the experimental data.

Restricting the drift gas of an IMS to helium or hydrogen, however, is problematic. Rokushika et al. [24] give reasons why the use of other gases might be not only desirable but also necessary. For this reason, the work described in this paper was conducted to study further the issues associated with sampling solvated ions with IMS/MS. The drift gases selected for the study were air and argon. Because these two gases have large Joule–Thomson expansion coefficients (0.1371 and 0.23, respectively, at 373 K) compared with helium (−0.0638 at 373 K) [25], any tendencies toward nucleation should be amplified (in agreement with Zook and Grimsrud). [22] Furthermore, because purified air is a commonly used drift gas for IMS, the ability to identify the ions with IMS/MS is of paramount importance. The urgency for the work increased when solvated ions in local equilibrium were found to contribute to the operation of a newer form of IMS (namely, RF–IMS) [26].

2. Experimental

Spangler and Carrico [27] have described an earlier version of the IMS/MS instrument that was used for the study. A proprietary stacked-ring IMS cell was coupled to an EXTRANUCLEAR (or EXTREL) quadrupole mass spectrometer. Since that earlier work, the stacked-ring IMS cell was replaced with a ceramic IMS cell and modifications were made to the mass spectrometer to improve its performance. The newer configuration is shown in Fig. 1.

An EXTREL CM-50 quadrupole mass analyzer is now used to analyze the ions, and a second turbomolecular pump replaces the 4-in diffusion pump of the earlier work. The ion-focusing lenses are still the same and focus the ions passing through a 25-micron sampling pinhole onto the entrance aperture of the mass spectrometer. The pinhole is electrically biased at ground potential, the pole zero for the quadrupole mass analyzer at ±20.7 V DC (depending on ion polarity), and the series of electrostatic lenses at ±36.3, ±9.0, ±63.0, ±18.7, and ±29.0 volts DC, respectively. Attached to the first lens is a cylindrical wire basket that extends out toward the ion-sampling pinhole. This wire basket gently samples and directs the flow of ions toward the ion-focusing lens assembly and removes gas from the immediate region of the expansion to reduce the effects of collisions. Fig. 2 shows a SIMION plot of the electric field within the wire basket [28]. The field increases from 4 V/cm immediately behind the pinhole to 16 V/cm 1.4 cm downstream from the pinhole, to 0 V/cm just before the ions enter the lens assembly. The measured quantity of gas entering the pinhole is 5.3 cc(RTP)/min, and the pinhole (along with its mounting flange) is heated to the temperature of the IMS cell to assure isothermal operations. The ion distributions did not change with the temperature of the pinhole.

The IMS cell is a ceramic IMS that is assembled on a stainless steel flange coupled to the vacuum housing of the mass spectrometer. Structurally, the cell consists of three parts: first, the reactor (4.4 cm long, 2.5 cm internal diameter); second, the drift tube (11.4 cm long, 3.8 cm internal diameter, 11.08 megohm resistance); and third, the membrane inlet (OV-101 impregnated microporous Teflon, 1.3 cm^2 area)

The three parts are stacked on top of each other to construct the cell and are held in place by four stainless steel rods threaded into the mounting flange.

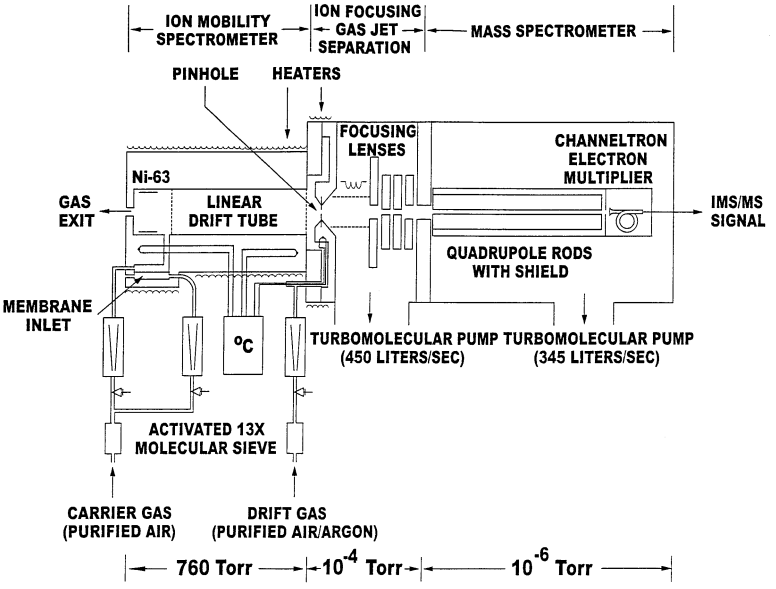

Fig. 1. Ion-mobility spectrometer/mass spectrometer (IMS/MS) used for this work. The ion-mobility spectrometer is on the left along with a gas conditioning system used to precondition the carrier and drift gases, the ion-sampling pinhole and vacuum interface is in the middle, and the quadrupole mass spectrometer is on the right. The vacuum system is differentially pumped with the ion-focusing lens assembly being maintained at 10^{-4} with a 450 L/s turbomolecular pump, and the quadrupole mass spectrometer was maintained at 10^{-6} Torr with a 345 L/s turbomolecular pump.

Teflon washers or ceramic tape are impregnated with OV-17 silicone oil to electrically insulate and seal the cell against the infusion of ambient air.

The cell components are machined from Macor glass-ceramic. Fired onto the internal surface of the reactor is a conductive thick-film ink (Heraeous-Cermalloy) that provides electrical contact to a 15 milliCurie ^{63}Ni radioactive source. Fired onto the internal surface of the drift tube is a resistive thick-film ink (Heraeous-Cermalloy, West Conshohocken, PA, USA) that serves as a linear resistor to create a drift field [29]. These thick films extend out to the outer surface of the IMS and terminate onto thick-film conduction pads for electrical contact. The aperture and shutter grids are photoetched grids (Buckbee-Mears, St. Paul, MN, USA) that are embedded in the conductive pads before final firing. Applied to the radioactive source is ±2478 V DC, ±1938 (high) and ±1908 (low) V DC are applied to the parallel-plane shutter grid, and ±127 V DC is applied to the aperture grid. Because IMS spectra can be collected through the mass spectrometer, no ion collector is included in the design of the IMS cell. Difficulties with the pulsed-shutter grid prevented collection of IMS spectra during the present effort.

The drift gas was introduced into the IMS by first flowing it between the mounting flange for the IMS and the vacuum flange of the mass spectrometer and then using it as a curtain gas for the ion-sampling pinhole before entering the cell. The drift gas later joined the carrier gas near the shutter grid and exhausted the cell after flowing through the reactor. Before mixing with the drift gas, the carrier gas flowed past an OV-101 impregnated membrane that served as a semipermeable membrane inlet for sample introduction purposes. The drift gas flow was typically 350 cc/min; the carrier (inside membrane) and sample (outside membrane) gas flows were typically 250 cc/min each. Thermocouples placed near the mounting flange (drift), reactor, and membrane inlet monitored the IMS temperature at these locations. The cell and pinhole were heated to 55°C with heater tapes powered by DC power supplies.

The purified air was processed from house air

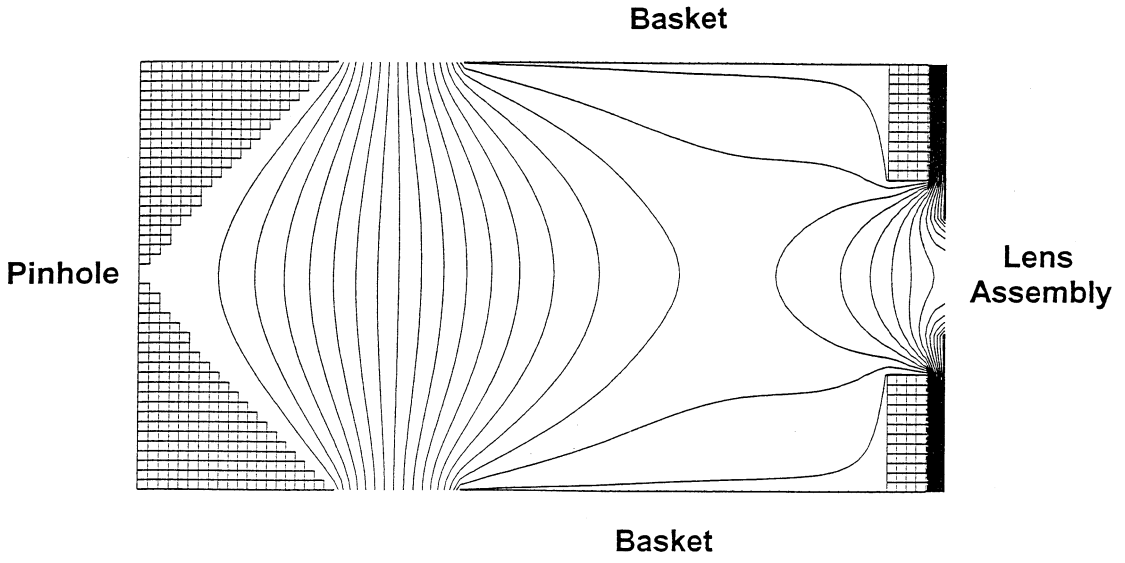

Fig. 2. SIMION plot of the electric field immediately behind the pinhole and within the ion-extracting wire basket. The field strength is 4 V/cm immediately behind the pinhole (left), increases to 16 volt/cm 1.42 cm downstream from the pinhole (center left), and decreases to near zero before the stronger focusing fields of the lens assembly (right) focuses the ions onto the entrance aperture of the mass spectrometer.

using a Balston (Lexington, MA, USA) CO_2 remover (two molecular sieve traps used in an automatic pressure-swing cycle). This CO_2 remover reduced the water concentration to ~3.5 ppm. The UN 1006 argon was tank gas provided by Matheson. Both gases were further processed through activated 13X molecular sieve traps (<8 h service) that had been previously baked at 300°C for 24 h using a purge of dry nitrogen. The mass spectrometer results showed that the activated molecular sieve traps were effective in further reducing the water concentration, as well as the CO_2 concentration, in the gases delivered to the IMS/MS. The water content of the gases was differentially measured using a DuPont 303 moisture monitor both before they entered and after they left the IMS cell, and the concentration was determined using the known response characteristics for the phosphorous pentoxide sensor. No data were collected until the measured moisture levels were the same at both the inlet and the outlet.

The mass spectra were collected with the aid of a Technivent PC-SPEC data acquisition system that allowed averaging of data. The data were collected with a 5-ms dwell time per peak, and multiple spectra were added and averaged so that well over 30 min of data are associated with each figure of this paper.

3. Results

3.1. Effectiveness of the 13X molecular sieve trap

Fig. 3 shows total ion mass spectra (the mass spectrum of all the ions generated in the reactor of the IMS with the pulsed shutter grid biased open to continuously conduct ions) collected when purified air was used for the sample, carrier, and drift gases without a 13X molecular sieve trap. The water content of the purified air was <3.4 ppm (the mass spectrometer data indicated 0.62 ppm), but the exact value was not determined by a differential measurement with the moisture monitor. The mass-to-charge (*m/z*) ratios for the major positive reactant ions are 55, 73, 83, 101, 111, and 129, which correspond to the hydronium ion with water and nitrogen adducts, $H_3^+O(H_2O)_n(N_2)_m$. This assignment is consistent with that of Kim et al. and was confirmed independently by Spangler and Carrico [27,30,31]. The most abundant ion of the

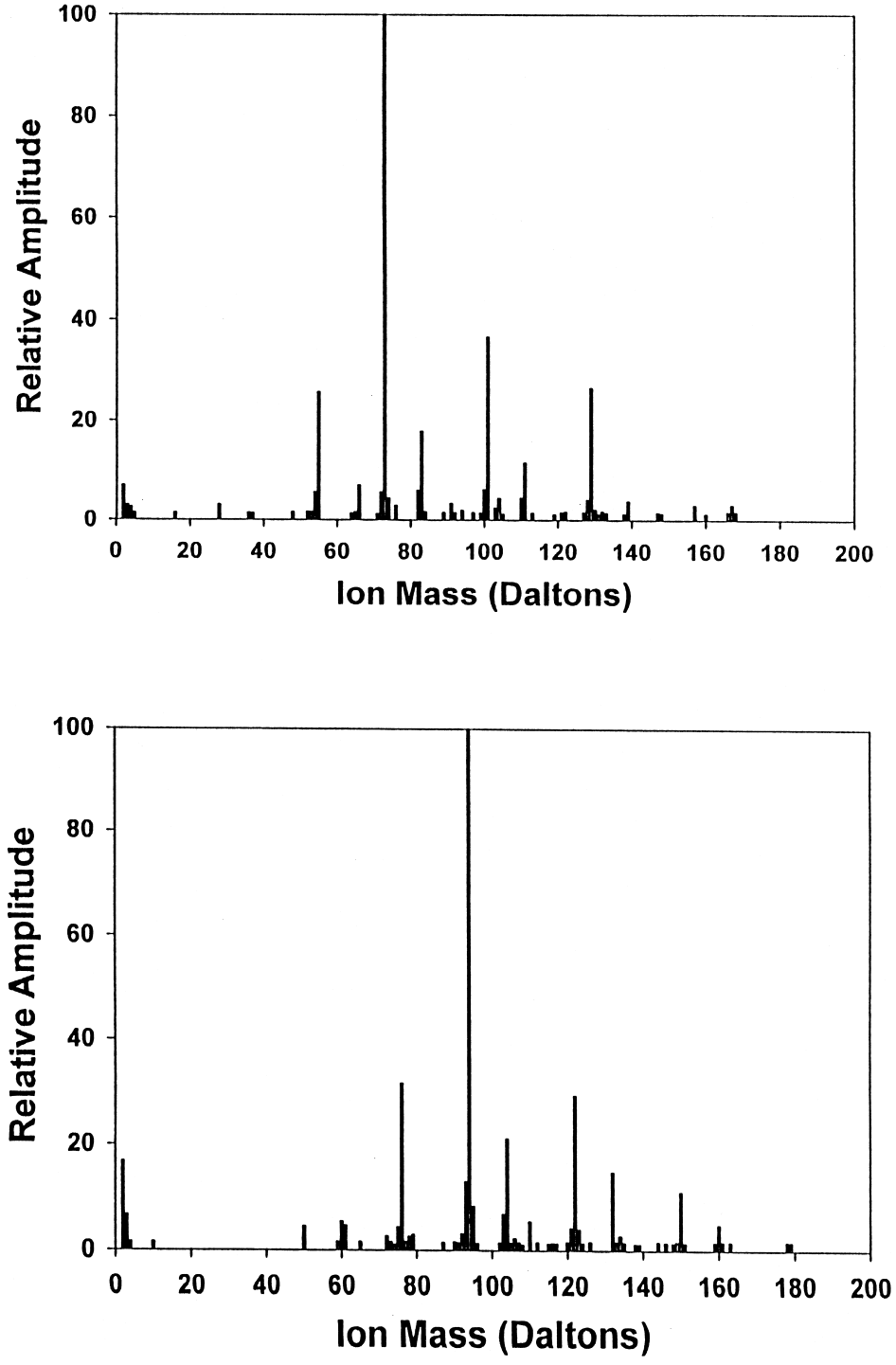

Fig. 3. Total ion mass spectra collected on the positive (top) and negative (bottom) reactant ions when purified air was used for the sample, carrier, and drift gases without an activated 13X molecular sieve trap. The temperature of the IMS cell was 328 K, and the water content of the purified air was 3.4 ppm.

series is $H_3O^+(H_2O)_3$, which has an amplitude 2.9 times that for $H_3O^+(H_2O)_2$ and 20 times that for $H_3O^+(H_2O)_4$. The *m/z*) ratios for the major negative reactant ions are 76, 94, 104, 122, 132, and 150, which correspond to $CO_4^-(H_2O)_n(N_2)_m$. This assignment is consistent with those of Spangler and Carrico but differs from that of Carr because of incomplete elimination of CO_2 by the purified-air generator [27,32,33]. The most abundant ion is $CO_4^-(H_2O)$, which has an amplitude 3.16 times that for CO_4^- and 68.2 times that for $CO_4^-(H_2O)_2$. For both the positive and negative ions, the relative amplitudes for the nitrogen adducts decrease with increasing mass of the ion. With few exceptions, this relationship is generally observed for all the data and can be used to assist in interpreting the mass spectra [27].

Fig. 4 shows total ion mass spectra that were collected using purified air for the sample, carrier, and drift gases after it was processed through an activated 13X molecular sieve trap. The water content of the purified air was 0.089 ± 0.005 ppm. The major positive reactant ions have *m/z* ratios of 37, 55, 73, 83, 101, 111, 129, 139, 147, which again correspond to the hydronium ion with water and nitrogen adducts, $H_3^+O(H_2O)_n(N_2)_m$ [27,30,31]. The most abundant ion is $H_3O^+(H_2O)_2$, which has an amplitude 4.12 times that for $H_3O^+(H_2O)$ and 1.95 times that for $H_3O^+(H_2O)_3$.

The major negative reactant ions have *m/z* ratios of 50, 60, 68, and 78, which correspond to $O_2^-(H_2O)_n(N_2)_m$; 64, 82, 92, 110, and 120, corresponding to $O_4^-(H_2O)_n(N_2)_m$; and 76, 94, and 104, corresponding to $CO_4^-(H_2O)_n(N_2)_m$. Because of the removal of CO_2 by the 13X molecular sieve trap, these assignments are more consistent with Carr than with Spangler and Carrico [27,32,33]. The most abundant ion in the O_2^- series is $O_2^-(H_2O)$, with an amplitude 13.2 times that for O_2^- and 7.45 times that for $O_2^-(H_2O)_2$. The most abundant ion in the O_4^- series is $O_4^-(H_2O)$, with an amplitude 2.89 times that for O_4^- and 13.2 times that for $O_4^-(H_2O)_2$. The most abundant ion in the CO_4^- series is CO_4^-, with an amplitude 2.70 times that for $CO_4^-(H_2O)$. The ions containing carbon dioxide constitute ~28% of the total ion current, compared with 100% in Fig. 3.

3.2. Studies with argon

Fig. 5 shows total ion mass spectra collected immediately before argon was introduced into the IMS cell. Purified air processed through an activated 13X molecular sieve trap was used for the carrier and drift gases, and ambient air was used for the sample gas. The water content of the purified air (before adding water through the membrane inlet) was 0.34 ± 0.02 ppm. The major positive reactant ions are $H_3O^+(H_2O)_n(N_2)_m$, with *m/z* ratios of 55, 73, 83, 101, 111, 129, 139, and 167 [27,30,31]. The most abundant ion of the series is $H_3O^+(H_2O)_3$, which has an amplitude 1.06 times that for $H_3O^+(H_2O)_2$ and 13.3 times that for $H_3O^+(H_2O)_4$. When the amplitude ratios are compared with those of Fig. 4, evidence for water permeation through the membrane inlet into the carrier gas is present. Ammonium ions $NH_4^+(H_2O)_n(N_2)_m$ also contribute to the data where the major ions have *m/z* ratios 36, 54, 72, 82, 100, 110, and 138. This assignment corresponds to that of Kim et al. and confirmed independently by Spangler and Carrico [27,30]. The most abundant ion is $NH_4^+(H_2O)_3$, which has an amplitude 1.17 times that for $NH_4^+(H_2O)_2$ and 11.5 times that for $NH_4^+(H_2O)_4$. The ammonium ions constitute ~18% of the total ion current.

The major negative reactant ions have *m/z* ratios of 50, 60, 68, and 78, corresponding to $O_2^-(H_2O)_n(N_2)_m$; 64, 82, 92, 110, and 120, corresponding to $O_4^-(H_2O)_n(N_2)_m$; and 76, 94, and 104, corresponding to $CO_4^-(H_2O)_n(N_2)_m$ [27,32,33]. The most abundant ion for the O_2^- series is $O_2^-(H_2O)$, with an amplitude 14.7 times that for O_2^- and 1.83 times that for $O_2^-(H_2O)_2$. The most abundant ion for the O_4^- series is $O_4^-(H_2O)$, with an amplitude 3.87 times that for O_4^- and 10.1 times that for $O_4^-(H_2O)_2$. The most abundant ion for the CO_4^- series is CO_4^-, with an amplitude 2.29 times that for $CO_4^-(H_2O)$. The O_4^- ions are more abundant in Fig. 5 than in Fig. 4 (suggesting possible contributions from NO_2^-), and the ions containing carbon dioxide constitute ~12% of the total ion current. The ion series starting at *m/z* 60 may indicate the presence of CO_3^-, but this is not firmly established [32]. Contributions from CO_3^- are not included in the carbon dioxide budget stated above.

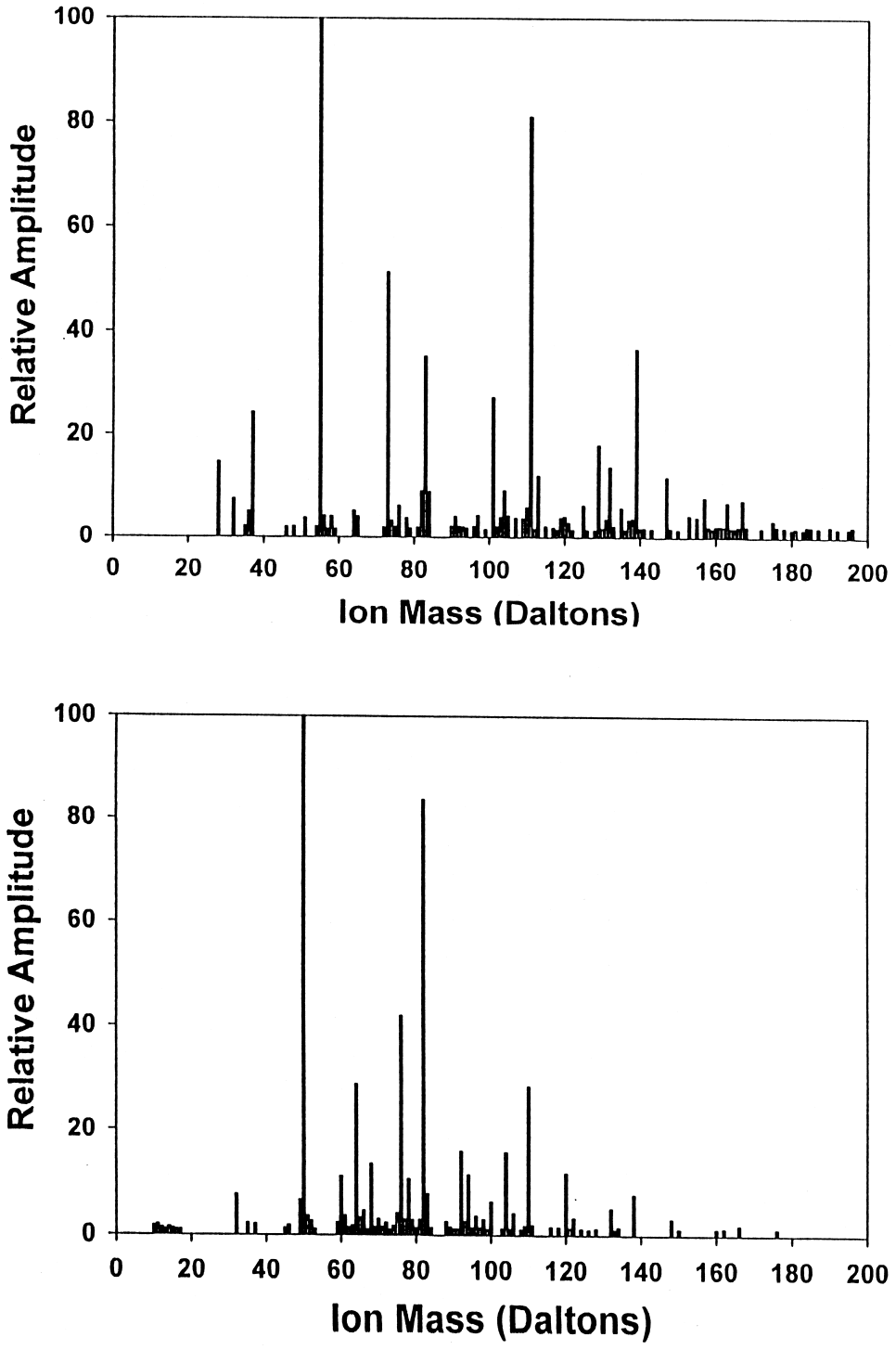

Fig. 4. Total ion mass spectra that were collected on the positive (top) and negative (bottom) reactant ions when purified air was used for the sample, carrier, and drift gases after being processed through an activated 13X molecular sieve trap. The temperature of the IMS cell was 328 K, and the water content of the purified air was 1.16 ppm.

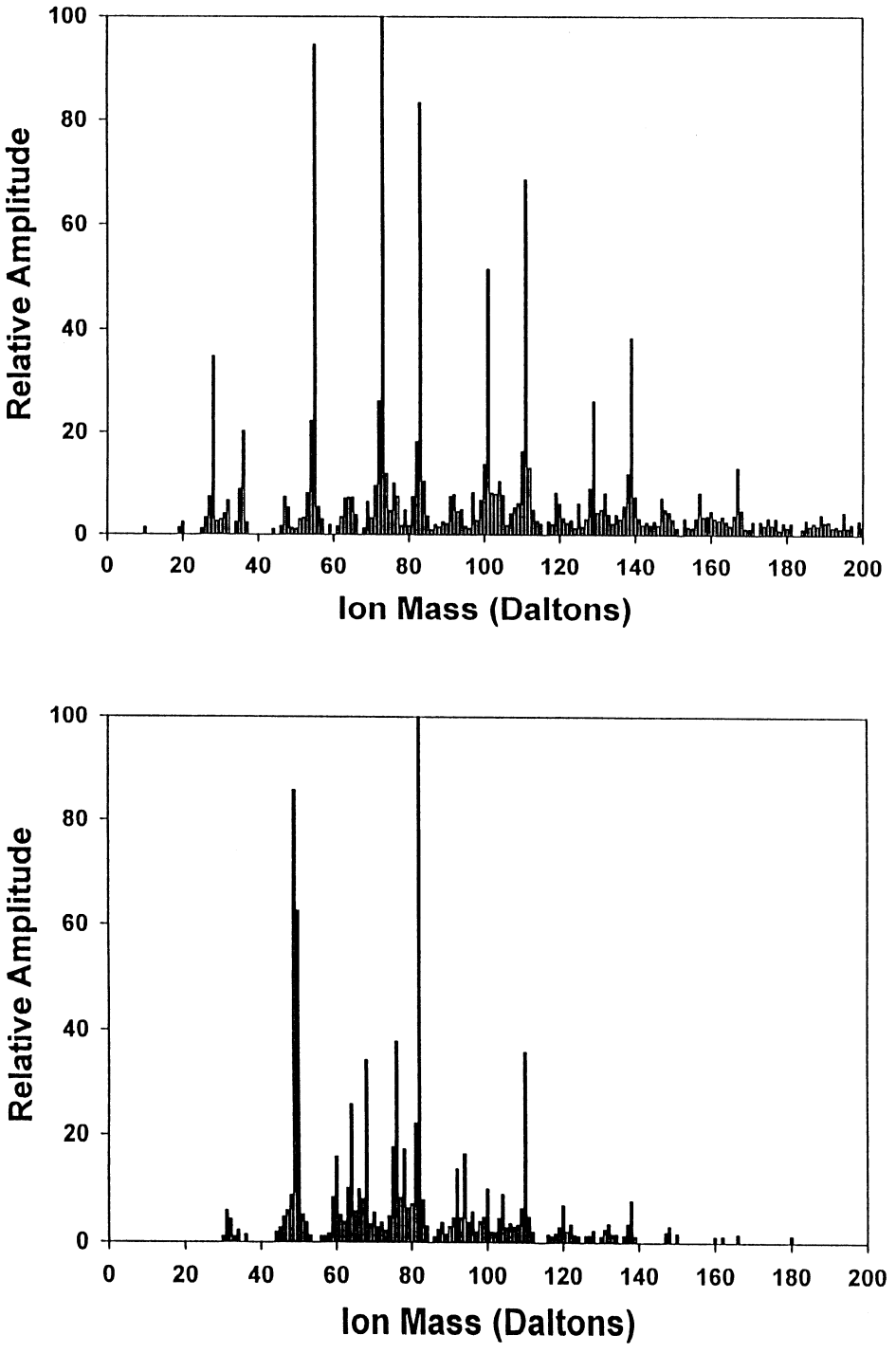

Fig. 5. Total ion mass spectra that were collected on the positive (top) and negative (bottom) reactant ions while using purified air for the carrier and drift gases processed through an activated 13X molecular sieve trap and while using ambient air for the sample gas. The temperature of the IMS cell was 328 K, and the water content of the purified air was 1.06 ppm.

Fig. 6 shows total ion mass spectra that were collected using purified air processed through an activated 13X molecular sieve trap for carrier gas, argon processed through an activated 13X molecular sieve trap for drift gas, and ambient air for sample gas. The water content of the purified air was 1.06 ± 0.30 ppm, with the water content of the argon being probably slightly higher because of the aged condition (>8 h service) of the molecular sieve trap used in combination with that gas. The major positive reactant ions are $H_3O^+(H_2O)_n(N_2)_m$, with *m/z* ratios of 37, 55, 73, 83, 91, 101, 111, 119, 129, 139, 157, and 167. The most abundant ion of the series is $H_3O^+(H_2O)_3$, which has an amplitude 2.02 times that for $H_3O^+(H_2O)_2$ and 8.84 times that for $H_3O^+(H_2O)_4$. The ammonium ions $NH_4^+(H_2O)_n(N_2)_m$ also appear at masses *m/z* 36, 54, 72, 74, 82, 100, 102, 110, 130, and 158. The most abundant ion of the ammonium series is $NH_4^+(H_2O)_3$, which has an amplitude 1.42 times that for $NH_4^+(H_2O)_2$ and 5.22 times that for $NH_4^+(H_2O)_4$. Argon makes its contribution to masses 39–40 and adducts to $H_3O^+(H_2O)(N_2)_m$, $m = 0, \ldots, 3$, at *m/z* 77, 105, and 133; and to $H_3O^+(H_2O)_3(N_2)_m$, $m = 1, \ldots, 3$, at *m/z* 113 (weak), 141, and 169. The major negative reactant ions have mass-to-charge ratios of 50, 60, 68, 78, 96, 106, 124, 134, 152, 162, 180, and 190 corresponding, to $O_2^-(H_2O)_n(N_2)_m$; 64, 82, 92, 100, 110, 118, 120, 128, 136, 138, 146, 148, 156, 164, 166, corresponding to $O_4^-(H_2O)_n(N_2)_m$; and 76, 94, 104, 122, 132, 140, 150, 160, 168, and 178, corresponding to $CO_4^-(H_2O)_n(N_2)_m$. The most abundant O_2^- ion is $O_2^-(H_2O)_2$, which has an amplitude 1.38 times that for $O_2^-(H_2O)$ and 10.53 times that for $O_2^-(H_2O)_3$. The most abundant O_4^- ion is $O_4^-(H_2O)$, with an amplitude 9.22 times that for O_4^- and 1.47 times that for $O_4^-(H_2O)_2$. The most abundant CO_4^- ion is $CO_4^-(H_2O)$, with an amplitude 2.05 times that for CO_4^- and 10.73 times that for $CO_4^-(H_2O)_2$. In addition, argon adducts possibly make contributions to the following sets of negative ion masses (the leading italicized head mass having the identity noted above): *82*, 122, 162; *68*, 108, 148; *110*, 150, 190; *94*, 134, 174; *50*, 90; *100*, 140, 180; *96*, 136, 176; *78*, 118; *122*, 162, 202; *106*, 146; and *124*, 164. Thus the identity of the ions with *m/z* values 134, 162, 180 and 190 in the $O_2^-(H_2O)_n(N_2)_m$ series are uncertain because they potentially contain argon adducts of the other ions, Similarly the identity of the ions with *m/z* values 118, 136, 146, 148, 164 and 122, 140, 150 in the $O_4^-(H_2O)_n(N_2)_m$ and the $CO_4^-(H_2O)_n(N_2)_m$ series, respectively, are uncertain. Although $O_4^-(H_2O)$, *m/z* 82, is the most abundant negative ion in Figure 6, the uncertain mass assignments do not allow statements relating to the relative concentration of ions to be made. Finally, the ion series starting with *m/z* 60 may contain CO_3^-.

Fig. 7 shows total ion mass spectra that were collected using argon processed through an activated 13X molecular sieve trap for carrier and drift gases and ambient air for sample gas. The water content of the argon was ~1.06 ppm. The major positive reactant ions are $H_3O^+(H_2O)_n(N_2)_m$, with *m/z* ratios of 55, 73, 83, 101, and 111. The most abundant ion of the series is $H_3O^+(H_2O)_3$, which has an amplitude 1.95 times that for $H_3O^+(H_2O)_2$ and 10.86 times that for $H_3O^+(H_2O)_4$. The ammonium ions $NH_4^+(H_2O)_n(N_2)_m$ are also still present at masses *m/z* 36, 54, 72, and, perhaps, 74. The most abundant ammonium ion is $NH_4^+(H_2O)_3$, which has an amplitude 1.41 times that for $NH_4^+(H_2O)_2$ and 18.65(?) times that for $NH_4^+(H_2O)_4$. Argon makes a contribution to masses 39–40, as well as adducts to the hydrated hydronium and ammonium ions. The major negative reactant ions have *m/z* ratios of 60, 100, 140, and 180, corresponding to $CO_3^-(Ar)_n$. These ions are thought to contain no contributions from $O_2^-(N_2)_m$ because of the absence of $O_2^-(H_2O)_n(N_2)_m$, $n>0$, in the spectrum. The most abundant ion is CO_3^-, which has an amplitude 2.87 times that for $CO_3^-(Ar)$. The total ion current for the CO_3^- ions in Fig. 7 is ~18% of the total negative ion current in Figs. 5 and 6.

3.3. Tandem mass spectrometry (MS/MS) data

Because MS/MS data were not collected during this work, the above mass assignments are made without benefit of the capabilities provided by that instrumentation. The assignments, however, are made after many years of experience with the operation and performance of the instrument. Consequently, it is

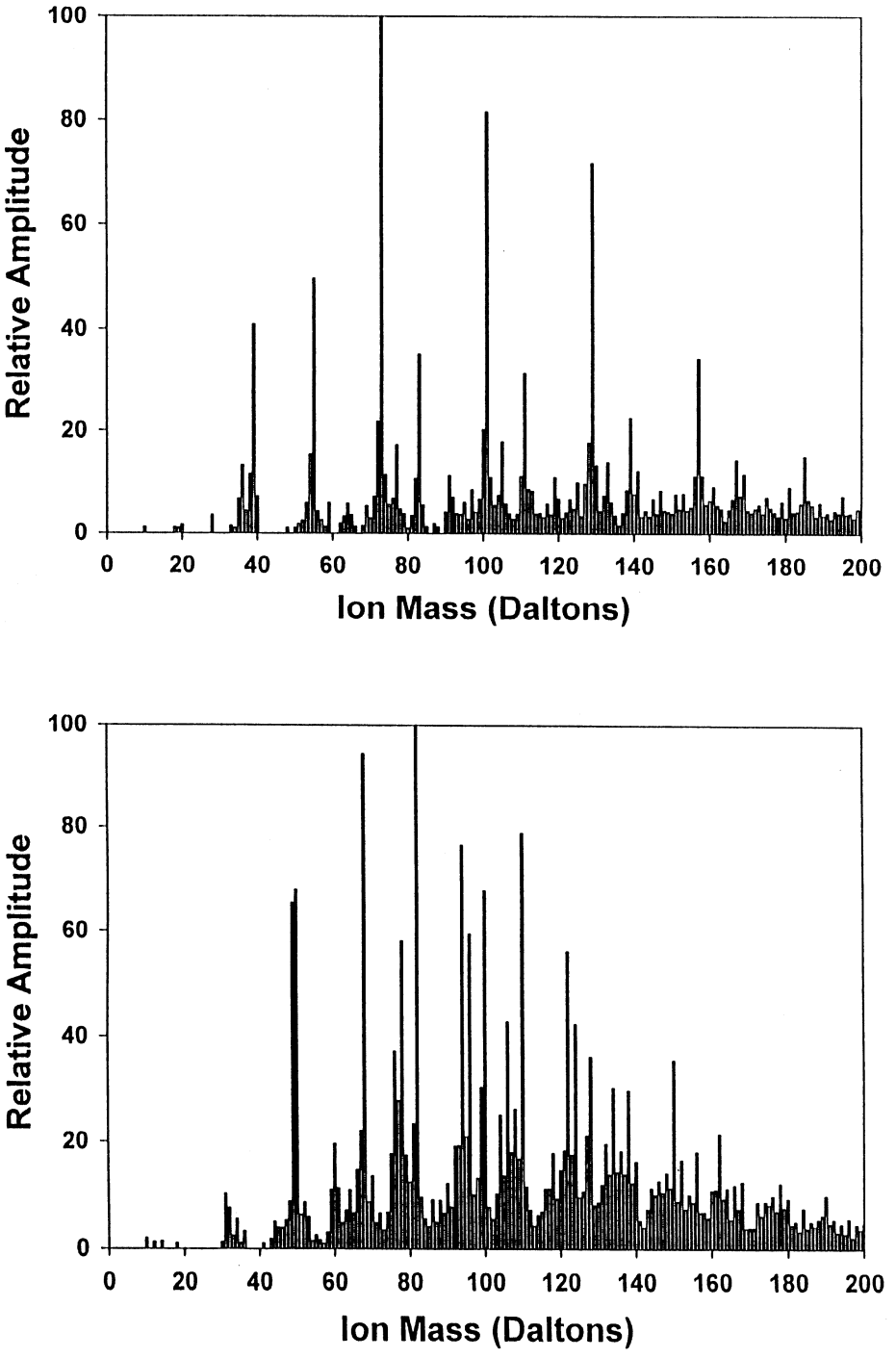

Fig. 6. Total ion mass spectra that were collected on the positive (top) and negative (bottom) reactant ions while using purified air processed through an activated 13X molecular sieve trap for carrier gas, argon processed through an activated 13X molecular sieve trap for drift gas, and ambient air for sample gas. The temperature of the IMS cell was 328 K, and the water content of the purified air and argon was 1.06 ppm (plus any water that entered the carrier gas through the membrane inlet).

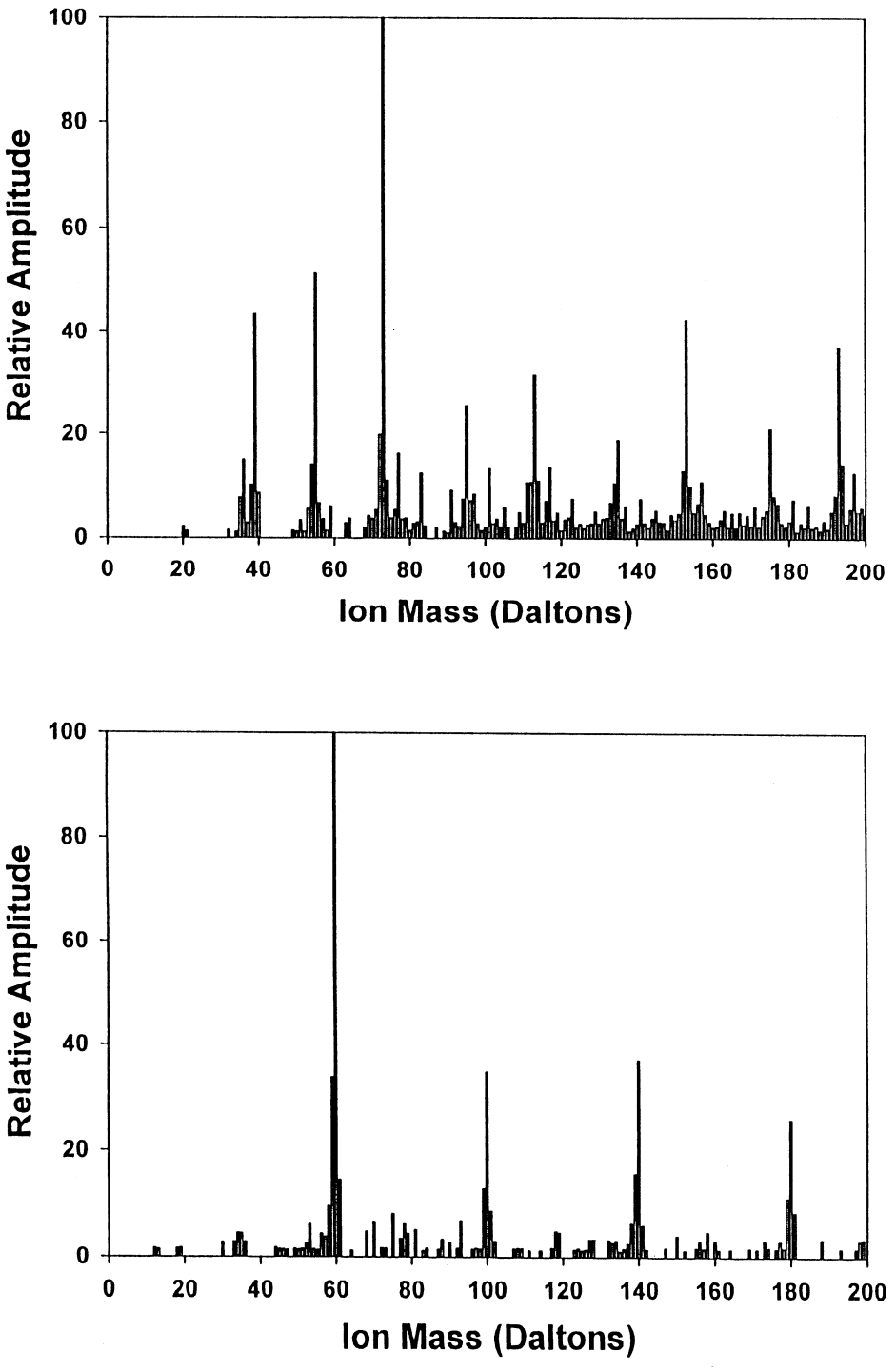

Fig. 7. Total ion mass spectra that were collected on the positive (top) and negative (bottom) reactant ions while using argon processed through an activated 13X molecular sieve trap for carrier and drift gases and while using ambient air for sample gas. The temperature of the IMS cell was 328 K, and the water content of the purified air was 1.06 ppm (plus any water that entered the carrier gas through the membrane inlet).

believed that the assignments are reasonably accurate, with a slight chance that some of the assignments are erroneous. An attempt has been made to provide alternative identifications for those assignments at greatest risk. While tandem mass spectrometry might clarify the assignments (particularly for the higher-mass ions) [34], most tandem mass spectrometers use a skimmer, not a wire basket, to sample ions. The author's experience is that this can significantly change the composition of the ions recorded by the mass spectrometer. Furthermore, redundancy in adducts for a given core ion (e.g., O_2^-, H_3O^+, or NH_4^+) confuses parent/daughter relationships.

4. Discussion

4.1. Effusion into the vacuum system

The pinhole interface between the IMS and mass spectrometer can be viewed as a constant area duct or nozzle with a diameter $D = 25$ microns and a length $L = 1.0$ mil (25 microns). The measured 5.3 cc(RTP)/min flow rate through the nozzle equates to a linear velocity of 180 m/s corresponding to a Mach number of 0.54. As air and argon are compressible gases, their flow can be analyzed using a Fanno line analysis that assumes friction with (isothermal) or without (isoentropic) heat addition [35]. For isothermal flow, the Fanno line analysis indicates that the pressure drops 51 Torr as the gas passes through the pinhole. For isoentropic flow, the Fanno line analysis indicates that the pressure drops 5 Torr and the temperature drops 0.2 K as the gas passes through the pinhole. As it was demonstrated experimentally that the data are not altered by the temperature of the pinhole (see section 2), the isoentropic flow result is favored over the isothermal flow result. Consequently, the thermodynamics associated with the ions passing through the pinhole affect little the composition of the ions entering the vacuum system of the mass spectrometer. The time spent by the ions in the pinhole is on the order of 80 nanoseconds, with a Reynolds number of 303.

This result differs from the analysis of Miller [36], who claims that the source exit, or "throat," is choked at Mach 1 and the exit pressure drops to the stagnant pressure, P_0, divided by a critical parameter $G = ([\gamma + 1]/2)^{\gamma/(\gamma-1)}$, where γ is the specific heat ratio (C_p/C_v) [36]. For the present experiments, the Fanno line ratio fL/D (f = friction coefficient) is small because of the short length of the pinhole. As a result, the gas exiting the pinhole is not choked.

4.2. Free jet expansion

Once in the vacuum, the gas expands adiabatically and forms a free jet [36–38]. The density of the gas and the gas kinetic temperature of the jet decrease until the speed of the flow eventually exceeds that of the local speed of sound. The expanding zone (sometimes referred to as the zone of silence) is surrounded by a concentric barrel shock and may be terminated, in addition, by a perpendicular shock, known as the Mach disc. Ashkenas and Sherman [37] locate the Mach disc at x_m

$$\frac{x_m}{D} = 0.67\left(\frac{P_0}{P_1}\right)^{1/2}, \tag{1}$$

downstream from the orifice, where P_1 is the background pressure for the expansion within the cylindrical wire basket.

The background pressure P_1 can be estimated by using

$$\frac{1}{S} = \frac{1}{F} + \frac{1}{S}, \tag{2}$$

where S is the rate with which the wire basket is evacuated, S_p is the pumping speed for the turbomolecular pump (450 L/s), and F is the conductance of the wire basket (assumed to be many small orifices in parallel). Equating SP_1 to the rate of gas flow entering the vacuum through the pinhole yields a background pressure of 1.1×10^{-3} Torr. This corresponds to a value of 1.4 cm for x_m, which locates the Mach disc immediately before the ions enter the cylindrical wire basket of Fig. 2. The time required for the ion to travel from the pinhole to the Mach disc is $\sim$19 μs.

The Mach number M for the gas flow is given by using 1.4 for γ [37–39].

$$M(x/D) = 3.65(x/D)^{2/3} - 0.82(x/D)^{-2/3} + \ldots, \quad (3)$$

where x is the location downstream from the pinhole. Since, for isotropic expansion, the translational temperature T of the gas is related to the Mach number through [40],

$$\frac{T_0}{T} = 1 + \frac{\gamma - 1}{2}M^2, \quad (4)$$

where T_0 is the translational temperature of the stagnant drift gas, and the translational temperature for the expanding gas just before it exits the Mach disc is near 0 K. As pointed out by Miller [36], this condition may never be reached, as the mean free path for the gas must remain within the geometric constraints of the apparatus. The lowest translational temperature achievable is probably on the order of 5 K (or greater if the shock wave thickness is also to remain approximately equal to the mean free path). As a result, a smooth transition probably occurs between continuum adiabatic expansion and free molecular flow [20].

4.2. Shifting equilibrium

Poisson's law can be used to describe the adiabatic portion of the expansion [41]

$$\frac{P_0}{P} = \left(\frac{T_0}{T}\right)^{\frac{\gamma}{\gamma-1}}. \quad (5)$$

Eq. (5) corresponds to the following pressure–temperature curve

$$\frac{dP}{dT} = \left(\frac{\gamma}{\gamma - 1}\right)\frac{P}{T}. \quad (6)$$

During the expansion, the ion clusters entrained in the expanding gas also attempt to equilibrate in accordance with

$$I^{\pm}(S)_{n-1} + S + M \rightleftharpoons I^{\pm}(S)_n + M, \quad (7)$$

where $I^{\pm}$ is the ion, S is the solvent molecule, and M is the collision partner (required to carry away the energy of reaction). The chemical thermodynamics describing the equilibrium are [42]

$$\Delta G^0_{n-1,n} = \Delta G_{n-1,n} - \Delta G^{\theta}_{n-1,n}$$

$$= -RT\, ln\, \frac{P_{I^{\pm}(S)_n} P_{STP}}{P_{I^{\pm}(S)_{n-1}} P_S}$$

$$= -RT\, ln\, K_{n-1,n}, \quad (8)$$

where $\Delta G_{n-1,n}$ ($= \Delta H_{n-1,n} - T\Delta S_{n-1,n}$, where $\Delta H_{n-1,n}$ is the enthalpy change and $\Delta S_{n-1,n}$ is the entropy change) is the change in free energy for the solvation reaction; $\Delta G^{\theta}_{n-1,n}$ ($= \Delta H^{\theta}_{n-1,n} - T\Delta S^{\theta}_{n-1,n}$, where $\Delta H^{\theta}_{n-1,n}$ is the standard enthalpy change and $\Delta S^{\theta}_{n-1,n}$ is the standard entropy change) is the change in free energy for the standard state (one atmosphere pressure); $\Delta G^0_{n-1,n}$ ($= \Delta H^0_{n-1,n} - T\Delta S^0_{n-1,n}$) is the net change in free energy relative to the standard state for the solvation reaction; P_X is the partial pressure of X for X equal to $I^{\pm}(S)_{n-1}$, $I^{\pm}(S)_n$ or S; P_{STP} is the standard pressure; R is the gas constant; and $K_{n-1,n}$ is the equilibrium constant [25]. Whenever the solvent (e.g., water) is a homogeneous mixture within the expanding gas, the partial pressure of the solvent satisfies $P_S = x_S P$, where x_S is the factional contribution of the solvent to the total pressure. Substituting this relationship into Eq. (8) and differentiating, another relationship for the pressure–temperature curve is obtained:

$$\frac{dP_{\infty}}{dT} = -\left(\frac{\Delta G^0_{n-1,n}}{R}\right)\frac{P}{T^2} \quad (9)$$

where P_{∞} designates an apparent pressure indicated by the thermochemistry. The ratio of the slope for the apparent to the pneumatic pressure (Eq. [6] and [9]) is

$$\frac{dP_{\infty}/dT}{dP/dT} = -\left(\frac{\gamma - 1}{\gamma}\right)\frac{\Delta G^0_{n-1,n}}{RT} \quad (10)$$

where the free energy change is negative for exothermic reactions. Because the apparent pressure P_{∞} decreases more rapidly with temperature than does the pneumatic pressure P, a chemically mediated nonequilibrium flow is soon established. Once this oc-

curs, the thermodynamic and fluid mechanical aspects of the problem become coupled, and more complex differential equations are needed to describe the expansion [43].

4.3. Nonequilibrium with sudden freezing

Three theoretical approaches to describing the nonequilibrium flow are available; namely, analytical, numerical, and semiempirical [44]. The most accurate are the numerical approaches, and the more complex are the analytical approaches [36]. Whenever they apply, the semiempirical approaches are simpler and provide a reasonably accurate description for the expansion. The most successful semiempirical approach is the "sudden freezing" approximation, in which equilibrium flow is assumed to be upstream of an empirically chosen freezing point, and frozen flow is assumed to be downstream from that point.

The onset of frozen flow arises from a balance between the flow dynamics and the chemical composition (including vibrational energy states [45]) of the system. For coupled chemical reactions, the onset of freezing can be described by [44]

$$\left| \rho V \sum_{i=n_a+1}^{n} \frac{g_{ir}}{W_i} \frac{dc_i}{dx} \right|_e \leq (R_{f,r})_e \simeq (R_{b,r})_e, \qquad (11)$$

where the reaction r is close to equilibrium (denoted by the subscript e). The left-hand side of Eq. (10) relates to the flow conditions where ρ and V are the density and linear velocity of the expanding gas, respectively; n, c_i and W_i are the number, mass fraction, and molecular weight of the reacting species, respectively; n_a is the number of equations describing the atomic aspects of the reactions; and g_{ir} depends on the stoichiometric coefficients. $R_{f,r}$ and $R_{b,r}$ on the right-hand side are the forward and backward fluxes (equal for equilibrium). Because the thermochemistry associated with each of the reactions r is different, the reactions freeze at different locations within the expansion. After freezing, the expansion continues as an adiabatic expansion without a shifting equilibrium.

Before the chemical changes that occur within an expansion can be described, a reaction mechanism must be defined. The kinetics for the solvation reaction of Eq. (7) satisfy

$$\frac{dP_{I^{\pm}(S)_{n-1}}}{dt} = -k_f P_{I^{\pm}(S)_{n-1}} P_S P + k_r P_{I^{\pm}(S)_n} P \qquad (12)$$

where k_f is the forward reaction rate constant [46–49] and k_r is the reverse reaction rate constant. The discussions of the previous paragraph suggest that at the point where sudden freezing occurs, the first derivative of Eq. (12) should be equal to zero, and

$$k_f P_{I^{\pm}(S)_{n-1}} P_S = k_r P_{I^{\pm}(S)_n}. \qquad (13)$$

Assuming that the ion currents $[I^{\pm}(S)_n]$ and $[I^{\pm}(S)_{n-1}]$ measured with the mass spectrometer are proportional to $P_{I^{\pm}(S)_n}$ and $P_{I^{\pm}(S)_{n-1}}$, Eq. (13) states

$$\frac{[I^{\pm}(S)_n]}{[I^{\pm}(S)_{n-1}]} = P_S \frac{k_f}{k_r} = \frac{P_S}{P_{STP}} \exp\left(- \frac{\Delta G^0_{n-1,n}}{RT} \right), \qquad (14)$$

where Eq. (8) has been applied to introduce the free energy. Assuming $P_S = x_S P$, where x_S is the mole fractional concentration of solvent in the expanding gas and the 0.08–1.0 ppm of water in the expanding gas does not change significantly during the expansion (a simplifying assumption that is generally applied for a free jet expansion with a trace constituent), Eq. (5) and (14) can be combined to yield

$$\frac{[I^{\pm}(S)_n]}{[I^{\pm}(S)_{n-1}]} = x_s \left(\frac{T}{T_0} \right)^{\frac{\gamma}{\gamma-1}} \exp\left(- \frac{\Delta G^0_{n-1,n}}{RT} \right). \qquad (15)$$

Plotted in Fig. 8 are the temperatures (relative to T_0 = 328 K) calculated from Eq. (15) when the amplitude ratios of Figs. 3, 4, and 5 are used for $\frac{[I^{\pm}(S)_n]}{[I^{\pm}(S)_{n-1}]}$ and thermodynamic data published by Kebarle [50] are used for $\Delta G^0{}_{n-1,n}$. These temperatures correspond to the freezing point where the dynamic equilibrium for the ions freezes out. The reproducibility of the ion intensity ratio divided by the mole fractional concentration of the solvent (water) is on the order of 53% for these data.

For each of the solvation systems

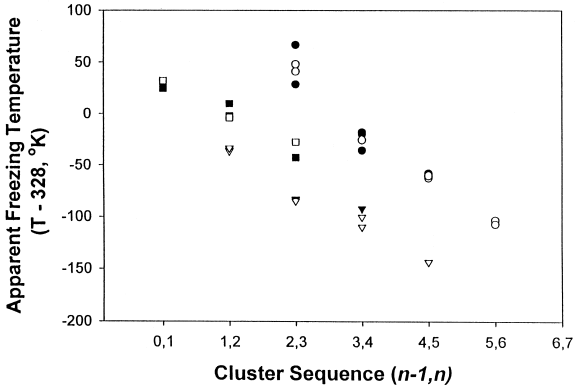

Fig. 8. Apparent temperature (relative to 328 K) at which the reactions of Eq. (17) are frozen before the product ions are sampled by the mass spectrometer. The solvation reactions relating to the hydronium ion (adducts assumed attached to protons) are indicated by circles, the ammonium ion by inverted triangles, and the oxygen anion by squares. The filled data points were collected while using purified air for the drift gas; open data points were collected while using argon for the drift gas.

$$H^+(H_2O)_{n-1} + H_2O + M \rightleftharpoons H^+(H_2O)_n + M; \quad (16)$$

$$NH_4^+(H_2O)_{n-1} + H_2O + M \rightleftharpoons NH_4^+(H_2O)_n + M; \quad (17)$$

$$O_2^-(H_2O)_{n-1} + H_2O + M \rightleftharpoons O_2^-(H_2O)_n + M, \quad (18)$$

where M is a collision partner, the rate of decrease of the freezing temperature with adduct addition is approximately linear with the number of adducts. According to Fig. 8, freezing occurs further downstream for larger ion clusters. This is because of the lower free energy associated with forming these ions.

An inconsistency in the data is the freezing temperature for the reaction

$$H^+(H_2O)_2 + H_2O + M \rightleftharpoons H^+(H_2O)_3 + M, \quad (19)$$

which is greater than 328 K, the stagnant drift gas temperature. Because the deviation defies a physical explanation, the data were reanalyzed for possible sources of error. A statistical treatment of the data showed that the data points in Fig. 8 were reproducible to within ±7 K. When the sensitivity of the freezing temperature to the water content (x_S) of the expanding gas was studied, Eq. (15) indicated that a water content of 0.067 ppm (slightly less than the measured experimental value) was needed if the reaction was to proceed at room temperature and that a freezing temperature of 352–376 K was needed if the water content was to be 1 ppm. Because the water concentration was shown to be significant from this analysis, the moisture monitor data were reanalyzed. This led to revised values for the water concentration, but further lowering the water concentration was not justified. Consequently, another explanation for the inconsistently high temperature of Fig. 8 was needed.

The nature of the inconsistency was further studied using Eq. (14). As $\Delta G^0_{n-1,n}$ is negative for reaction (19), the elevated temperatures of Fig. 8 correspond to a reduced concentration for the higher–molecular weight ion relative to the lower–molecular weight ion in the exchanging clusters. That is, the ratio $\frac{[I^{\pm}(S)_n]}{[I^{\pm}(S)_{n-1}]}$ is lower than expected for a reaction that is assumed to occur at stagnant drift gas temperature. With this information, the task became to explain the decrease in this ratio, or a reason why Eq. (14) should not be used to perform the above analysis.

Addressing the limitations of Eq. (14) first, the theory for free jet expansion assumes that equilibria can shift during an expansion but also acknowledges that nonequilibrium conditions can also develop. For example, it is known that each of the cluster reactions "freezes out" at different locations within the expansion, giving rise to a variety of subtle processes within the complex expanding jet. All these processes are lumped together by the semiempirical sudden freezing approximation that was used to calculate the freezing temperatures of Fig. 8. Because of this lumping, one cannot be sure that the calculated freezing points will always agree with experimentally measured values.

Laying this aside, a search was made for mechanisms whereby the relative ion concentrations can be explained. Three were identified: virtual impaction, limited reaction kinetics, and collisional dissociation. Differences in ion momenta lead to selective ion sampling because of a phenomenon known as virtual impaction, which arises both from the ions entering

the vacuum system with a characteristic momentum and from the conservation of momentum allowing the higher–molecular weight ions to be sampled preferentially over lower–molecular weight ions. To illustrate, let $\vec{v}_{CM}$ and $\vec{v}_{rel}$ be the (vector) velocities for the center of mass and the relative motion of gas molecules and ions as they expand into the vacuum system, respectively [51]. Then as collisions occur between the ions and the expanding gas molecules, $\vec{v}_{rel}$ will change, but $\vec{v}_{CM}$ will not change. These velocities are given by

$$\vec{v}_{CM} = \frac{M_{ion}\vec{v}'_{ion} + M_{mol}\vec{v}'_{mol}}{M_{ion} + M_{mol}}; \tag{20}$$

$$\vec{v}'_{rel} = \vec{v}'_{ion} - \vec{v}'_{mol}, \tag{21}$$

where $\vec{v}'_{ion}$ and $\vec{v}'_{mol}$ are the final velocities for the ion (with mass M_{ion}) and gas molecule (with mass M_{mol}) after the collision, respectively, in the laboratory frame of reference. When Eq. (20) and (21) are rearranged,

$$\vec{v}'_{ion} = \vec{v}_{CM} + \frac{M_{mol}\vec{v}'_{rel}}{M_{ion} + M_{mol}}; \tag{22}$$

$$\vec{v}'_{mol} = \vec{v}_{CM} - \frac{M_{ion}\vec{v}'_{rel}}{M_{ion} + M_{mol}}. \tag{23}$$

Eq. (22) states that the higher-mass ion travels with a velocity more like the center-of-mass velocity than a lower-mass ion. Because an equation similar to Eq. (20) can also be written for the motion before the collision, the higher-mass ion also dictates the direction of the motion. The net result is that a higher-mass ion travels a straighter path than a lower-mass ion when entering the vacuum system of the mass spectrometer. For the present experiments, the path is a straight path from the ion-sampling pinhole to the entrance aperture of the mass spectrometer. The situation is similar to inertial impaction of aerosol particles onto a solid disc [52,53], except that the disc is a hole (virtual disc) corresponding to the entrance aperture of the mass spectrometer.

Two problems are encountered when attempting to explain the present results with virtual impaction. The first is that heavier ions are enriched over lighter ions, the opposite of what is needed to explain the decreased value for the ratio $\frac{[I^{\pm}(S)_n]}{[I^{\pm}(S)_{n-1}]}$. The second is that all the heavy ions in Fig. 8 should be equally affected. This is contrary to the fact that the heavier O_2^- and $O_2^-(H_2O)$ ions are not preferentially sampled over the $H^+(H_2O)_2$ and $H^+(H_2O)_3$ ions in Fig. 8.

A variation on the virtual impaction theme is skimmer technology. A skimmer is a sampling orifice that is introduced behind the ion-sampling pinhole of an atmospheric pressure ionization mass spectrometer to preferentially sample high–molecular weight ions (along with managing pressure distributions within the interface manifold). Because skimmer technology was not used to generate the present data, low mass discrimination should not be observed. However, a less pronounced discrimination might occur because of preferences in the radial expansion of the gas. As the time scale associated with this radial expansion is long, allowing the composition of the ion clusters to readjust to the expansion conditions, one cannot be sure that skimmer-like activity did not contribute to the data. One thing is certain: the contribution is much less than that occurring in other atmospheric pressure ionization mass spectrometers equipped with a skimmer.

Limited reaction kinetics can allow equilibrium reactions to become imbalanced during an expansion. From this point of view, two time constants are associated with the kinetics described by Eq. (12); namely, the forward τ_f and reverse τ_r time constants:

$$\tau_f = \frac{0.693}{k_f P_S P} \qquad \tau_r = \frac{0.693}{k_r P}. \tag{24}$$

Because the equilibrium constant of Eq. (8) satisfies

$$K_{n-1,n} = \frac{k_f P_{STP}}{k_r} = \frac{\tau_r P_{STP}}{\tau_f P_S} = \exp\left[-\frac{\Delta G^0_{n-1,n}}{RT}\right], \tag{25}$$

the reverse time constant also satisfies

Table 1
Kinetic data for the forward reactions associated with the expansion

Reaction	k_f cm^6/mol^2 s	$\tau_f(P_0, T_0)$ sec	$T(\tau_f = 19\ \mu s)$ K
$H_3O^+ + H_2O + O_2 \rightarrow H^+(H_2O)_2 + O_2$[a]	3.7×10^{-27}	1.7×10^{-6}	233
$H_3O^+ + H_2O + N_2 \rightarrow H^+(H_2O)_2 + N_2$[b]	3.4×10^{-27}	1.9×10^{-6}	236
$H^+(H_2O)_2 + H_2O + O_2 \rightarrow H^+(H_2O)_3 + O_2$[a]	2.0×10^{-27}	3.2×10^{-6}	254
$H^+(H_2O)_2 + H_2O + N_2 \rightarrow H^+(H_2O)_3 + N_2$[b]	2.3×10^{-27}	2.8×10^{-6}	249
$H^+(H_2O)_3 + H_2O + O_2 \rightarrow H^+(H_2O)_4 + O_2$[a]	2.0×10^{-27}	3.2×10^{-6}	254
$H^+(H_2O)_3 + H_2O + H_2 \rightarrow H^+(H_2O)_4 + N_2$[b]	2.4×10^{-27}	2.7×10^{-6}	248
$H^+(H_2O)_4 + H_2O + O_2 \rightarrow H^+(H_2O)_5 + O_2$[a]	0.9×10^{-27}	7.2×10^{-6}	285
$O_2^- + H_2O + O_2 \rightarrow O_2^-(H_2O) + O_2$[c]	2.2×10^{-28}	29×10^{-6}	349
$O_2^- + H_2O + O_2 \rightarrow O_2^-(H_2O) + O_2$[d]	1.6×10^{-28}	40×10^{-6}	365
$O_2^- + H_2O + O_2 \rightarrow O_2^-(H_2O) + O_2$[e]	3.0×10^{-28}	22×10^{-6}	334
$O_2^-(H_2O) + H_2O + O_2 \rightarrow O_2^-(H_2O)_2 + O_2$[c]	6.0×10^{-28}	11×10^{-6}	302
$O_2^-(H_2O) + H_2O + O_2 \rightarrow O_2^-(H_2O)_2 + O_2$[d]	5.4×10^{-28}	12×10^{-6}	307
$O_2^-(H_2O) + H_2O + O_2 \rightarrow O_2^-(H_2O)_2 + O_2$[e]	4.0×10^{-28}	16×10^{-6}	320

[a] [54].
[b] [55].
[c] [49].
[d] [56].
[e] [57].

$$\tau_r = \frac{\tau_f P_S}{P_{STP}} \exp\left[-\frac{\Delta G^0_{n-1,n}}{RT} \right] = \frac{0.693}{k_f P_{STP} P} \exp\left[-\frac{\Delta G^0_{n-1,n}}{RT} \right]. \quad (26)$$

Finally, the relationship $P_S = x_S P$ and Eq. (5) allow [2]

$$\tau_f = \frac{0.693}{k_f x_S P_0^2} \left(\frac{T_0}{T} \right)^{\frac{2\gamma}{\gamma-1}} \quad (27)$$

$$\tau_r = \frac{0.693}{k_f P_0^2} \left(\frac{T_0}{T} \right)^{\frac{\gamma}{\gamma-1}} \exp\left(-\frac{\Delta G^0_{n-1,n}}{RT} \right). \quad (28)$$

The time constants of Eq. (27) and (28) are a maximum under stagnant gas temperature ($T = T_0$) and pressure ($P = P_0$) conditions. These maximum values are recorded in Tables 1 and 2. Data for only the hydrated hydronium cation and the hydrated oxygen anion are shown because of a lack of published rate constant data for the other ions [46–49]. A water concentration of 0.214 parts per million (average of the values reported in this paper) was used for the calculations.

A critical situation develops when the reverse time constant, as recorded in Table 2, becomes greater than the residence time (19 μs) for the ions in the expansion. The equilibrium no longer restores itself as imbalances develop within the expansion. The translational temperature where this time constant becomes equal to the residence time is recorded in the last column of Table 2. Restoration of the equilibria is possible only when this recorded temperatures is less than the stagnant drift gas temperature. A review of Tables 1 and 2 shows that a shifting equilibrium occurs only for the reactions

$$H^+(H_2O)_3 + H_2O + M \rightleftharpoons H^+(H_2O)_4 + M; \quad (29)$$

$$H^+(H_2O)_4 + H_2O + M \rightleftharpoons H^+(H_2O)_5 + M; \quad (30)$$

$$O_2^-(H_2O) + H_2O + M \rightleftharpoons O_2^-(H_2O)_2 + M, \quad (31)$$

where M may be O_2 or N_2. For these reactions, the forward and reverse time constants are both less than the residence time for the ions in the expansion.

It is important to note that the reaction of Eq. (19) is not included in reactions (29)–(31). In Table 1, the forward time constant for this reaction is 2.8–3.2 μs, and in Table 2, the reverse time constant is 0.55–0.63 ms. Because the reverse time constant is longer, and the forward time constant is shorter, than the resi-

Table 2
Kinetic data for the reverse reactions associated with the expansion

Reaction	$k_r(P_0, T_0)$ cm^3/molec sec	$\tau_r(P_0, T_0)$ sec	$T(\tau_r = 19\ \mu s)$ K
$H_3O^+ + H_2O + O_2 \leftarrow H^+(H_2O)_2 + O_2$[a]	8.6×10^{-24}	3.6×10^{3}	524
$H_3O^+ + H_2O + N_2 \leftarrow H^+(H_2O)_2 + N_2$[b]	7.7×10^{-24}	4.0×10^{3}	525
$H^+(H_2O)_2 + H_2O + O_2 \leftarrow H^+(H_2O)_3 + O_2$[a]	4.0×10^{-17}	6.3×10^{-4}	355
$H^+(H_2O)_2 + H_2O + N_2 \leftarrow H^+(H_2O)_3 + N_2$[b]	5.6×10^{-17}	5.5×10^{-4}	354
$H^+(H_2O)_3 + H_2O + O_2 \leftarrow H^+(H_2O)_4 + O_2$[a]	1.6×10^{-13}	1.9×10^{-7}	281
$H^+(H_2O)_3 + H_2O + N_2 \leftarrow H^+(H_2O)_4 + N_2$[b]	2.1×10^{-13}	1.5×10^{-7}	279
$H^+(H_2O)_4 + H_2O + O_2 \leftarrow H^+(H_2O)_5 + O_2$[a]	2.1×10^{-11}	1.5×10^{-9}	254
$O_2^- + H_2O + O_2 \leftarrow O_2^-(H_2O) + O_2$[c]	6.3×10^{-17}	4.9×10^{-4}	368
$O_2^- + H_2O + O_2 \leftarrow O_2^-(H_2O) + O_2$[d]	4.6×10^{-17}	6.7×10^{-4}	373
$O_2^- + H_2O + O_2 \leftarrow O_2^-(H_2O) + O_2$[e]	8.6×10^{-17}	3.6×10^{-4}	364
$O_2^-(H_2O) + H_2O + O_2 \leftarrow O_2^-(H_2O)_2 + O_2$[c]	1.3×10^{-14}	2.3×10^{-6}	305
$O_2^-(H_2O) + H_2O + O_2 \leftarrow O_2^-(H_2O)_2 + O_2$[d]	1.2×10^{-14}	2.5×10^{-6}	306
$O_2^-(H_2O) + H_2O + O_2 \leftarrow O_2^-(H_2O)_2 + O_2$[e]	9.1×10^{-15}	3.4×10^{-6}	309

[a] [54].
[b] [55].
[c] [49].
[d] [56].
[e] [57].

dence time for the ions in the expansion, enrichment of the higher–molecular weight ion occurs. This again is opposite to that required for explaining the reduced ratio observed for $\frac{[I^{\pm}(S)_n]}{[I^{\pm}(S)_{n-1}]}$.

Finally, the electric field within the wire basket may dissociate the ions as they gain energy from the field and collide with neutral gas molecules during the expansion [58–62]. This may occur just beyond the Mach disc, where the density of the neutral gas molecules is still reasonably high, along with a reasonably high electric field (see Fig. 2). Collisional dissociation of larger cluster ions is favored over smaller cluster ions because the larger ions are more weakly bound to their final adducts. When these thoughts are applied to reaction (19), the decreased ratio for $\frac{[I^{\pm}(S)_n]}{[I^{\pm}(S)_{n-1}]}$ is now explained.

A problem with collisional dissociation is that it is at odds with the explanations that will be given later for the appearance of nitrogen and argon adducts in the mass spectra of Figs. 3–7. The problem arises because nitrogen and argon adducts are more weakly bound to their ions than are water adducts and should experience collisional dissociation before the water adducts do. A possible compromising position is that the nitrogen and argon adducts are formed further downstream within the wire basket, where both the pressure and the ion-focusing field are at a reduced level.

As the forward and reverse time constants associated with the reaction

$$O_2^- + H_2O + O_2 \rightleftharpoons O_2^-(H_2O) + O_2 \quad (32)$$

are both longer than the 19-μs residence time, the amplitude ratio for the $O_2^-(H_2O)$ and O_2^- ions should provide a reasonable estimate of the water concentration present in the stagnant drift gas. Assuming that this condition is independent of the collision partner (i.e., nitrogen instead of oxygen), the data of Figs. 4 and 5 imply 0.17 ppm for Fig. 4 and 0.19 ppm for Fig. 5, compared with the experimental measured values of 0.089 and 0.12 ppm, respectively. When the same analysis is done for the reactions

$$H^+(H_2O)_2 + H_2O + M \rightleftharpoons H^+(H_2O)_3 + M; \quad (33)$$

$$H^+(H_2O)_3 + H_2O + M \rightleftharpoons H^+(H_2O)_4 + M, \quad (34)$$

the water concentrations are found to be 0.0125 ppm (Fig. 4) and 0.122 ppm (Fig. 5) and 1.92 ppm (Fig. 4) and 3.96 ppm (Fig. 5), respectively. The higher

concentration that is derived using reaction (34) is probably related to the lower freezing temperature determined for this reaction (see Fig. 8).

A lesser amount of information exists for the ammonium ion clusters shown in Fig. 8. The relative placement of these ions suggests that the water adducts are more weakly bound to these ions than to the hydronium cation or oxygen anion. This is consistent with the higher proton affinity of ammonia. While some doubt exists for the relative magnitudes of the reaction rates, the freezing temperatures indicated in Fig. 8 are probably close to the temperature where the concentrations for these ions are finally established by sudden freezing.

4.4. Nitrogen adducts

When the analysis of the previous section is applied to the nitrogen adducts, the free energy of reaction is found to be endothermic (independent of temperature), contrary to the adducts' apparent stability within the mass spectrum. This implies either that condensation of nitrogen occurs within the zone of silence or that the nitrogen adducts are formed downstream from the Mach disc before they enter the mass spectrometer. Except for secondary evidence that will be presented in connection with the argon data, the present experimental setup did not provide clear evidence for the correct mechanism.

For purposes of argument, it can be assumed that the ions are formed downstream from the Mach disc, where the background pressure was approximately 1.1×10^{-3} Torr (P_S in Eq. [8]). With this assumption, it is found that $\Delta G_{m-1,m}/\mathrm{RT}$ has a value of -12.9 ± 0.6 for all the reactions

$$I^{\pm}(H_2O)_n(N_2)_{m-1} + N_2 + M \rightleftharpoons I^{\pm}(H_2O)_n(N_2)_m + M, \qquad (35)$$

where $I^{\pm}$ is the hydronium, ammonium cations, or oxygen anion, with m ranging from 1 to 4. That is, the binding energy is independent of the ion and the degree of clustering. Such a result suggests that a nonspecific reaction, such as the charge-induced dipole interaction, is responsible for the addition and that more specific reaction sites, such as nonbonded electrons, do not contribute.

Because the gas temperature downstream from the Mach disc was not known, it is not possible to accurately estimate $\Delta G^0{}_{m-1,m}$ from $\Delta G_{m-1,m}/\mathrm{RT}$. Even though Ferguson et al. have reported a forward rate constant of 4.0×10^{-32} cm^6 molecule^{-2} s^{-1} for the attachment of a nitrogen molecule to an oxygen anion [63,64], this, too, does not provide much information. For these reasons, the enthalpy was estimated from the interaction potential (minimum of the 12-6-4 Lennard-Jones potential [65]), using [66–69]

$$V_p = -\frac{\alpha q^2}{3r_m^4}, \qquad (36)$$

where α is the polarizability of nitrogen (1.74×10^{-24} cm^3 [70]), q is the electronic charge, and r_m is the radius of interaction. If the radius of interaction is assumed to satisfy [26,65,71]

$$r_m = 2^{2/3}(1.18 \cdot \sqrt[3]{V_{m,ion}} + \sigma_{nitrogen}) \qquad (37)$$

where $V_{m,\mathrm{ion}}$ is the molal volume for the ion and $\sigma_{\mathrm{nitrogen}}$ is the molecular diameter for nitrogen, then V_p equals approximately -1.2 kcal/mol for $H^+(H_2O)_3N_2$ for a radius of interaction of 5.11 Å [72]. When this value for V_p is used for $\Delta H^0{}_{m-1,m}$, the above value of -12.9 for $\Delta G^0{}_{m-1,m}/\mathrm{RT}$ corresponds to a temperature of 22 K and 0.5 kcal/mol for $\Delta G^0{}_{m-1,m}$. An entropy of 29 cal/K mol was used for the calculations.

When these values for $\Delta H^0{}_{m-1,m}$ and $\Delta G^0{}_{m-1,m}$ are extrapolated to the atmospheric operating conditions for the IMS, the nitrogen adducts are found to be only momentarily stable within the IMS. Their indicated lifetime is 13 ps, much less than 0.6 ns, which is the collision time between molecules under atmospheric pressure conditions. This means they are formed only within the vacuum system of the mass spectrometer (J.A. Stone, personal communication). While the error associated with this analysis is not easily estimated because of the number of assumptions going into the estimate, the conclusion seems to

be consistent with the results of Viehland et al. [73], who found that reduced mobilities generated by a FAIMS apparatus operated under atmospheric pressure conditions agree with those produced by a linear ion mobility spectrometer operated at reduced pressures [74]. Although the low field mobility (2.75 cm^2 V^{-1} s^{-1}) of Viehland et al. [70] does not agree with that of Karasek et al. (2.92 cm^2 V^{-1} s^{-1}) [75–78], minimal contributions from cluster adducts formed with the drift gas are indicated.

4.5. Argon

As the nitrogen drift and carrier gases are replaced with argon in the IMS, the reactant ions remain pretty much the same. The shifting equilibria for the hydrated hydronium ions and the energetics for the nitrogen adducts are similar, as demonstrated by Fig. 8, where the argon data nicely overlay the nitrogen data. The differences are that argon adducts are also formed and that the oxygen anions disappear when argon completely replaces purified air for both the carrier and drift gases.

Addressing first the hydronium ions, Good et al. [55] have proposed that the reactions leading to the hydrated hydronium ions in moist nitrogen are [79]

$$\begin{aligned} N_2 &\xrightarrow{60\ kev\ \beta} N_2^+ + e^-; \\ N_2^+ + 2N_2 &\rightarrow N_4^+ + N_2; \\ N_4^+ + H_2O &\rightarrow H_2O^+ + 2N_2; \\ H_2O^+ + H_2O &\rightarrow H_3O^+ + OH; \\ H_3O^+ + H_2O + N_2 &\rightarrow H^+(H_2O)_2 + N_2. \end{aligned} \tag{38}$$

On the basis of these reactions, it would seem that the reactant ion composition should either change or, even, disappear as the nitrogen is replaced with argon. For example, Adams et al. [80] noted that

$$\begin{aligned} Ar &\xrightarrow{67\ kev\ \beta} Ar^+ \\ Ar^+ + N_2 &\not\rightarrow N_2^+ + Ar, \end{aligned} \tag{39}$$

where the rate constant for the last reaction ranges in value from 1×10^{-11} cm^3 $molecule^{-1}$ s^{-1} for low argon concentration to 4×10^{-12} cm^3 $molecule^{-1}$ s^{-1} for high argon concentration. Figs. 6 and 7 do not show a decrease in hydrated hydronium ion concentration commensurate with reaction (39).

Lindinger et al. [81] and Smith et al. [82] report that the forward reaction for

$$Ar^+(^2P_{3/2}) + N_2 \underset{k_r}{\overset{k_f}{\rightleftharpoons}} Ar + N_2^+ \tag{40}$$

surprisingly proceeds by the endoergic $N_2^+(X,\nu = 1)$ product channel at 300 K and that k_r is large enough to cancel the effects of k_f. This implies that the reaction of Ar^+ with N_2 is fast. However, the charge transfer appears to be dependent on the geometry and the lifetime of the intermediate complex [83]. The presence of Ar^+ in Figs. 6 and 7 possibly could support the formation of the intermediate complex, provided $^2P_{3/2}$ is present and has a reasonable lifetime. Unfortunately, this probably does not occur. To reduce the collisional frequency associated with the reverse reaction and to stabilize the $^2P_{3/2}$ state, the preferred location for the reaction would be in the vacuum system of the mass spectrometer. Clearly, the vacuum environment of the mass spectrometer is significantly removed from the reactor of the IMS, a situation that casts doubt on whether reaction (40) plays a significant role in the formation of the hydronium ions.

Adams et al. [80] studied the reaction

$$Ar^+ + O_2 \rightarrow O_2^+ + Ar \tag{41}$$

and found it to be much faster than that for nitrogen. Because the data of Figs. 6 and 7 show no evidence for O_2^+, the involvement of reaction (41) is also questioned. Furthermore, reaction (41) suffers from all the arguments leveled against reaction (39) above, as the concentration of air is reduced in the IMS. If a significant source of oxygen exists in the mass spectrometer (an unlikely circumstance), perhaps the reaction could become important.

Another argument that is more consistent with the high-pressure operating conditions of the IMS is that Ar_2^+ is involved in forming the reactant ions. Bohme et al. [84] report that the reaction of Ar_2^+ with various diatomic molecules is very fast (10^{-10} cm^3 $molecule^{-1}$ s^{-1}). Unfortunately, they did not study the reaction of Ar_2^+ with nitrogen or water. However, they

did note that the reaction rates decrease with the exoergicity of the reaction. From this point of view, nitrogen has an ionization potential (15.6 eV) greater than that for carbon monoxide (14.0 eV), which is ionized by Ar_2^+ at a rate of 8.5×10^{-10} cm^3 molecule^{-1} s^{-1}. Because the ionization potential of nitrogen is also less than that for argon (15.76 eV), the reaction should be less exoergic than that with carbon monoxide and proceed with, essentially, unit probability. Although this argument relies heavily on two ionization potentials that are very close together, the formation of hydronium reactant ions by reaction of Ar_2^+ with water makes more sense than the reactions considered.

Addressing the nitrogen adducts, it is unlikely that they originate in the IMS. If they did, their concentration and distribution would change as the argon to nitrogen ratio changed. Consequently, the appearance of nitrogen adducts in the argon data indicates they are formed in the vacuum environment of the mass spectrometer. Within the vacuum environment, they could be formed either in the zone of silence or downsteam from the Mach disc. As the zone of silence contains a high concentration of argon and is protected by the shock barrier from the infusion of nitrogen, it is highly unlikely that the nitrogen adducts originate from reactions within this region. This means that the nitrogen adducts must originate downstream from the Mach disc, as already assumed in the discussion.

Further support for this is provided by the calculated free energies for the reactions. $\Delta G^0_{m-1,m}$/RT is equal to -13.4 ± 0.3 for the air carrier/argon drift data for Fig. 6, and -12.6 ± 0.6 for the argon carrier/argon drift data of Fig. 7. These values are close to those determined with air carrier and drift gases and are, again, independent of the degree of clustering.

Similar to the nitrogen adducts, the argon adducts are formed from reactions of the type

$$I^{\pm}(H_2O)_n(Ar)_{m-1} + Ar + M \rightleftharpoons I^{\pm}(H_2O)_n(Ar)_m + M. \quad (42)$$

The application of Eq. (8) again shows that the reactions are nonspecific and must occur beyond the Mach disc. They are further characterized by a value of -12.8 ± 0.6 for $\Delta G^0_{m-1,m}$/RT, a value strikingly similar to that for nitrogen. Because argon has a polarizability of 1.64×10^{-24} cm^3, a reasonable estimate for $\Delta H^0_{m-1,m}$ is -1.02 kcal/mol [70]. This value for $\Delta H^0_{m-1,m}$ indicates that nitrogen is more strongly attached to the ions than argon, explaining why nitrogen adducts are observed when argon is used for the drift gas.

Finally, unique to argon is the fact that the ions present in the mass spectrum cannot be unambiguously identified. The problem relates to an overlapping of masses between the various sequences of adducts. For example, in the positive-ion mode, $H^+(H_2O)_n(N_2)_m$ and $H^+(H_2O)_{n-2}(N_2)_{m-3}(Ar)_3$ have the same masses, as do $NH_4^+(H_2O)_n(N_2)_m$ and $NH_4^+(H_2O)_{n-2}(N_2)_{m-3}(Ar)_3$, $H^+(H_2O)_n(N_2)_{4m}$ and $H^+(H_2O)_{4m+n}(Ar)$, $NH_4^+(H_2O)_n(N_2)_{4m}$ and $NH_4^+(H_2O)_{4m+n}(Ar)$, and so forth, where n and m are variable parameters. In the negative-ion mode, $O_2^-(H_2O)_n(N_2)_m$ and $O_2^-(H_2O)_{n-2}(N_2)_{m-3}(Ar)_3$ have the same masses, as do $O_4^-(H_2O)_n(N_2)_m$ and $O_4^-(H_2O)_{n-2}(N_2)_{m-3}(Ar)_3$, $CO_4^-(H_2O)_n(N_2)_m$ and $CO_4^-(H_2O)_{n-2}(N_2)_{m-3}(Ar)_3$, $O_2^-(H_2O)_n(N_2)_{4m}$ and $O_2^-(H_2O)_{4m+n}(Ar)$, $O_4^-(H_2O)_n(N_2)_{4m}$ and $O_4^-(H_2O)_{4m+n}(Ar)$, $CO_4^-(H_2O)_n(N_2)_{4m}$ and $CO_4^-(H_2O)_{4m+n}(Ar)$, $O_2^-(H_2O)_n(N_2)_m$ and $CO_4^-(H_2O)_n(N_2)_{m-3}Ar$, $O_2^-(H_2O)_n(N_2)_m(Ar)_2$ and $O_4^-(H_2O)_{n-2}(N_2)_{m+3}$, $O_4^-(H_2O)_n(N_2)_{m-1}(Ar)$ and $CO_4^-(H_2O)_n(N_2)_m$, and so forth. It would seem that tandem mass spectrometry might help to sort out the identity of these ions. However, the commonality of adducts could frustrate such an effort. Fortunately, the problem is not as severe as initially thought, as higher-order clusters (large n or m) typically make a lesser contribution to a mass than a lower-order cluster (small n or m). For this reason, it has been possible to analyze the data, as described in this article.

Finally, the overlap of masses may explain why Zook and Grimsrud [22] observed a wider distribution of ions when using an argon buffer gas. A problem with this position, however, is that Zook and Grim-

srud did not report nitrogen adducts in the presence of a nitrogen buffer gas as would be required to fully support the argument.

5. Conclusions

Except for the nitrogen and argon adducts, the identity of the ions observed in this work are pretty much as expected. This is consistent with the open scientific literature where atmospheric pressure ionization mass spectrometry has been demonstrated to be a powerful technique for identifying higher molecular weight ions. However, when solvated ions are analyzed with the technique, the weak bonds associated with the ion adducts and the corresponding equilibria that are created lead to sampling errors that distort measured ion distributions. Differential freezing of the solvated ions leads to false information about the relative concentration of the solute present in the stagnant drift gas. Also, reactions downstream of the Mach disc can create ghost peaks caused by the formation of nitrogen and/or argon adducts.

Care must be taken in applying the above conclusions to an atmospheric pressure ionization mass spectrometer equipped with an ion skimmer. A skimmer enriches high-mass ions as a virtual impactor, and, as it is often located inside the shock barrel, reactions downstream of the Mach disc can be eliminated. The impact of a skimmer on the properties of the shock barrel is debated in the literature.

References

[1] Plasma Chromatograpy, T.W. Carr (Ed.), Plenum, New York, 1984.
[2] G.A. Eiceman, Z. Karpas, Ion Mobility Spectrometry, CRC Press, Boca Raton, FL, 1994.
[3] G.A. St. Louis, H.H. Hill Jr., Crit. Rev. Anal. Chem. 21 (1990) 321.
[4] H.H. Hill Jr., W.F. Siems, R.H. St. Louis, D.G. McMinn, Anal. Chem. 62 (1990) 1201A.
[5] G.A. Eiceman, Crit. Rev. Anal. Chem. 22 (1991) 17.
[6] J.E. Roehl, Appl. Spectrosc. Rev. 26 (1991) 1.
[7] J.I. Baumbach, G.A. Eiceman, Appl. Spectrosc. 53 (1999) 338A.
[8] G.E. Spangler, P.A. Lawless, Anal. Chem. 50 (1978) 884.
[9] A.P. Snyder, S.A. Liebman, M.A. Schroeder, R.A. Fifer, Org. Mass Spectrom. 25 (1990) 61.
[10] G.E. Spangler, A Study on the Stability of the $(M+NO_2)^-$ Ion for RDX in Ion Mobility Spectrometry, Proceedings of the 5th International Symposium on the Analysis and Detection of Explosives, Washington, DC, December 4−8, 1995, Paper 56.
[11] J.P. Carrico, S.H. Kim, G.E. Spangler, The Analysis of Bis(2-Chloroethyl)-Thioether Using Ion Mobility Spectrometry/Mass Spectrometry (IMS/MS), Technical Report, Contract DAAK11-80-C-0024, Chemical Systems Laboratory, Aberdeen Proving Ground, MD 21010, June 1982.
[12] S.H. Kim, G.E. Spangler, J. Epstein, A.W. Davis, The Analysis of Isopropyl and Pinacolyl Methylphosphono-Fluoridate Using Ion Mobility Spectrometry/Mass Spectrometry (IMS/MS), Report CRDEC-CR-88070, Chemical Research, Development and Engineering Center, Aberdeen Proving Ground, MD 21010, June 1988.
[13] A.P. Snyder, C.S. Harden, Org. Mass Spectrom. 25 (1990) 53.
[14] A.P. Snyder, C.S. Harden, Org. Mass Spectrom. 25 (1990) 301.
[15] S.N. Ketkar, S.M. Penn, W.L. Fite, Anal. Chem. 63 (1991) 457.
[16] C.S. Harden, A.P. Snyder, G.A. Eiceman, Org. Mass Spectrom. 28 (1993) 585.
[17] F.W. Karasek, H.H. Hill Jr., S.H. Kim, J. Chromatogr. 117 (1976) 327.
[18] S.H. Kim, G.E. Spangler, Analysis of Headspace Vapors of Marijuana and Marijuana Cigarette Smoke Using Ion Mobility Spectrometry/Mass Spectrometry, in Instrumentation for Trace Organic Monitoring, R.E. Clement, K.W.M. Siu, H.H. Hill Jr., (Eds.), Lewis Publishers, Boca Raton, FL, 1992.
[19] C.T.R. Wilson, Phil. Trans. R. Soc. 189 (1897) 265; ©C.T.R. Wilson, Phil. Trans. R. Soc. 193 (1899) 289.
[20] J.Q. Searcy, J.B. Fenn, J. Chem. Phys. 61 (1974) 5282.
[21] S.H. Kim, K.R. Betty, F.W. Karasek, Anal. Chem. 50 (1978) 2006.
[22] D.R. Zook, E.P. Grimsrud, J. Phys. Chem. 92 (1988) 6374.
[23] E.P.F. Lee, J.M. Dyke, A.E. Wilders, P. Watts, Mol Phys. 71 (1990) 207.
[24] S. Rokushika, H. Hatano, H.H. Hill Jr. Anal. Chem. 58 (1986) 361.
[25] J.H. Noggle, Physical Chemistry, Little, Brown, & Company, Boston, 1985.
[26] G.E. Spangler, Field Anal. Chem. & Technol., 4 (2000) 255.
[27] G.E. Spangler, J.P. Carrico, Int. J. Mass Spectrom. Ion Phys. 52 (1983) 267.
[28] Developed by D.C. McGilvery at LaTrobe University, Australia, and extensively modified by D.A. Dahl at Idaho National Engineering Laboratories, Idaho Falls, ID.
[29] G.E. Spangler, D.N. Campbell, K.N. Vora, J.P. Carrico, ISA Transactions 23 (1984) 17.
[30] S.H. Kim, F.W. Karasek, S. Rokushika, Anal. Chem. 50 (1978) 152.
[31] S.H. Kim, Fundamental Aspects of Plasma Chromatography, Ph.D. dissertation, University of Waterloo, Ontario, Canada, 1977.
[32] T.W. Carr, Anal. Chem. 49 (1977) 828.

[33] T.W. Carr, Anal. Chem. 51 (1979) 705.
[34] P.H. Dawson, Int. J. Mass Spectrom. Ion Phys. 43 (1982) 195.
[35] J.E.A. John, Gas Dynamics, Chapter 9, Prentice Hall, Englewood Cliffs, NJ, 1984.
[36] D.R. Miller, in Atomic and Molecular Beams, Vol. 1, Chapter 2, G. Scoles (Ed.), Oxford University Press, New York, 1988.
[37] H. Ashkenas, F.S. Sherman, in Rarefied Gas Dynamics, Fourth Symposium IV, Vol. 2 Section 7, J.H. DeLeeuw (Ed.), Academic Press, New York, 1966.
[38] D.J. Douglas, J.B. French, J. Anal. Atom. Spectrom. 3 (1988) 743.
[39] J.B. Anderson, in Molecular Beams and Low Density Gas Dynamics, Chapter 1, P.W. Wegener, (Ed.), Marcel Dekker, New York, 1974.
[40] A.H. Shapiro, The Dynamics and Thermodynamics of Compressible Fluid Flow, Vol. 1, Chapter 4, Wiley, New York, 1953.
[41] P.P. Wegener, in Heterogeneous Combustion, H.G. Wolfhard, I. Glassman, L. Green Jr. (Ed.), Academic Press New York, 1964, pp. 701–724.
[42] P. Kebarle, S.K. Searles, A. Zolla, J. Scarborough, M. Arshadi, J. Amer. Chem. Soc. 89 (1967) 6393.
[43] W.G. Vincenti, C.H. Kruger Jr., Introduction to Physical Gas Dynamics, Chapter 7, Krieger, Malabar, FL, 1986.
[44] K.N.C. Bray, in Gas Dynamics, Vol. 1. Nonequilibrium Flows, Part II, Chapter 3, P.P. Wegener (Ed.), Marcel Dekker, New York, 1970.
[45] T.L. Mazely, M.A. Smith, J. Phys. Chem. 94 (1990) 6930.
[46] E.E. Ferguson, F.C. Fehsenfeld, J. Geophys. Res., Space Phys. 74 (1969) 5743.
[47] R.S. Narcisi, W. Roth, Adv. Electron. Electron Phys. 29 (1970) 79.
[48] C.E. Young, W.E. Falconer, J. Chem. Phys. 57 (1972) 918.
[49] F.C. Fehsenfeld, E.E. Ferguson, J. Chem. Phys. 61 (1974) 3181.
[50] P. Kebarle, Ann. Rev. Phys. Chem. 28 (1977) 445.
[51] H. Massey, Atomic and Molecular Collisions, Chapter 1, Wiley/Halsted, New York, 1979.
[52] C.N. Davies, Proc. Inst. Mech. Eng. 1B (1952), 185.
[53] D.A. Lundgren, J. Air Pollution Control Assoc. 17 (1967) 225.
[54] A. Good, D.A. Durden, P. Kebarle, J. Chem. Phys. 52 (1970) 222.
[55] A. Good, D.A. Durden, P. Kebarle, J. Chem. Phys. 52 (1970) 212.
[56] J.D. Payzant, P. Kerbarle, J. Chem. Phys. 56 (1972) 3482.
[57] J.L. Pack, A.V. Phelps, Bull. Amer. Phys. Soc. 16 (1971) 214.
[58] G.H. Wannier, Phys. Rev. 83 (1941) 281; ©G.H. Wannier, Phys. Rev. 87 (1952) 795.
[59] L.A. Viehland, E.A. Mason, J.H. Whealton, J. Phys. B Atom. Molec. Phys. 17 (1974) 2433.
[60] L.A. Viehland, E.A. Mason, J. Chem. Phys. 66 (1977) 422.
[61] H. Kambara, Y. Mitsui, I. Kanomata, Anal. Chem. 51 (1979) 1447.
[62] Y. Mitsui, H. Kambara, M. Kojima, H. Tomita, K.Katoh, K. Satoh, Anal. Chem. 55 (1983) 477.
[63] N.G. Adams, D.K. Bohme, D.B. Dunkin, F.C. Fehsenfeld, E.E. Ferguson, J. Chem. Phys. 32 (1970) 3133.
[64] E.E. Ferguson, Accts. Chem. Res. 3 (1970) 402.
[65] E.A. Mason, H.W. Schamp, Ann. Phys. NY 4 (1958) 233.
[66] H. Eyring, J.O. Hirschfelder, H.S. Taylor, J. Chem. Phys. 4 (1936) 479.
[67] E.W. McDaniel, V. Cermak, A. Dalgarno, E.E. Ferguson, L. Friedman, Ion-Molecule Reactions, Wiley, New York, 1970.
[68] T. Su, M.T. Bowers, J. Chem. Phys. 58 (1973) 3027.
[69] D.R. Bates, Chem. Phys. Lett. 97 (1983) 19.
[70] CRC Handbook of Chemistry and Physics, D.R. Lide (Ed.); CRC Press, Boca Raton, FL, 1994.
[71] W.J. Lyman, W.F. Reehl, D.A. Rosenblatt, Handbook of Chemical Property Estimation Methods, McGraw-Hill, New York, 1982.
[72] L.I. Yeh, M. Okumura, J.D. Myers, J.M. Price, Y.T. Lee, J. Chem. Phys. 91 (1989) 7319.
[73] L.A. Viehland, R. Guevremont, R.W. Purves, D.A. Barnett, Int. J. Mass Spectrom. 197 (2000) 123.
[74] H. Bohringer, D.W. Fahey, W. Lindinger, F. Howorka, F.C. Fehsenfeld, D.L. Albritton, Int. J. Mass Spectrom. Ion Proc. 81 (1987) 45.
[75] F.W. Karasek, O.S. Tatone, Anal. Chem. 44 (1972) 1758.
[76] F.W. Karasek, O.S. Tatone, D.W. Denny, J. Chromatogr. 87 (1973) 137.
[77] F.W. Karasek, O.S. Tatone, D.M. Kane, Anal. Chem. 45 (1973) 1210.
[78] M.A. Baim, H.H. Hill Jr., J. High Resol. Chromatogr. Chromatogr. Comm. 6/1 (1983) 4.
[79] G.W. Griffin, I. Dzidic, D.I. Carroll, R.N. Stillwell, E.C. Horning, Anal. Chem. 45 (1973) 1204.
[80] N.G. Adams, D.K. Bohme, D.B. Dunkin, F.C. Fehsenfeld, J. Chem. Phys. 52 (1970) 1951.
[81] W.Lindinger, F. Howorka, P. Lukac, S. Kuhn, H. Villinger, E. Alge, H. Ramler, Phys. Rev. A23 (1981) 2319.
[82] D. Smith, N.G. Adams, Phys. Rev. A23 (1981) 2327.
[83] M.A. Smith, M. Hawley, in Advances in Gas Phase Ion Chemistry, Vol. 1, N.B. Adams, L.M. Babcock (Eds.), JAI Press, Greenwich, CT, 1992, pp. 167–202.
[84] D.K. Bohme, N.G. Adams, M. Mosesman, D.B. Dunkin, E.E. Ferguson, J. Chem. Phys. 52 (1970) 5094.